Nuclear Materials and Energy 40 (2024) 101698

Contents lists available at ScienceDirect

Nuclear Materials and Energy

journal homepage: www.elsevier.com/locate/nme

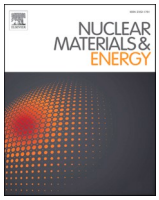

Hyperfine interactions of paramagnetic radiation-induced defect centres in advanced ceramic breeder pebbles

Andris Antuzevics [a,b], Arturs Zarins [c,d,*], Jekabs Cirulis [a], Andris Fedotovs [a], Anna Ansone [c], Magdalena Rzepna [e], Julia M. Leys [f], Regina Knitter [f]

[a] Institute of Solid State Physics, University of Latvia, 8 Kengaraga Str., LV-1063 Riga, Latvia
[b] Vilnius University, Institute of Chemistry, 24 Naugarduko Str., 03225 Vilnius, Lithuania
[c] University of Latvia, Institute of Chemical Physics, 1 Jelgavas Str., LV-1004 Riga, Latvia
[d] Daugavpils University, Faculty of Natural Sciences and Healthcare, 1A Parades Str., LV-5401 Daugavpils, Latvia
[e] Institute of Nuclear Chemistry and Technology, Centre for Radiation Research and Technology, Radiation Sterilization Plant for Medical Devices and Allografts, 16 Dorodna Str., 03-195 Warsaw, Poland
[f] Karlsruhe Institute of Technology, Institute for Applied Materials, 76021 Karlsruhe, Germany

ARTICLE INFO

Keywords:
Advanced ceramic breeder pebbles
Tritium breeding
Paramagnetic radiation-induced defect centres
Electron-nuclear double resonance
Electron paramagnetic resonance
Spectra simulations

ABSTRACT

Advanced ceramic breeder (ACB) pebbles consisting of 65 mol% lithium orthosilicate (Li_4SiO_4) and 35 mol% lithium metatitanate (Li_2TiO_3) are developed for tritium breeding in the European Union's (EU) helium cooled pebble bed (HCPB) breeder blanket concept of the demonstration fusion power plant (DEMO). Electron-nuclear double resonance (ENDOR) spectroscopy is a powerful and widely used magnetic resonance technique that combines aspects of electron paramagnetic resonance (EPR) and nuclear magnetic resonance (NMR). In the present work, ENDOR spectroscopy was applied to investigate hyperfine (HF) interactions of paramagnetic radiation-induced defect centres (containing unpaired electrons) in the biphasic ACB pebbles after irradiation with 10 MeV accelerated electrons. To separate individual EPR signals of the formed and accumulated paramagnetic centres, isochronal annealing of the irradiated ACB pebbles followed by EPR spectra measurements at X- and Q-microwave frequency bands at room and low temperature were performed. Afterwards, X-band ENDOR spectra at low temperature were recorded for selected EPR signals to reveal HF interactions between the unpaired electron spins with the spins of magnetic ^7Li and ^1H isotope nuclei. The g-factor and HF coupling values determined from EPR and ENDOR spectra simulations provide novel insights into the local structure of paramagnetic hole- and electron-type centres in the irradiated ACB pebbles.

Introduction

The demonstration fusion power plant (DEMO) will be the successor of the international thermonuclear experimental reactor (ITER), which is currently under construction at Cadarache, France, and is designed to explore the technical feasibility of fusion energy for commercial purposes [1]. DEMO will be operated as a steady-state electricity source with the aim to demonstrate the production of net electric power, operate with a closed tritium-deuterium fuel cycle, and qualify technological solutions for future commercial fusion power plants, including achieving the tritium self-sufficiency by nuclear transmutation reactions of lithium isotopes with neutrons produced in the deuterium–tritium fusion reactions [2]. The European Union's (EU) helium cooled pebble bed (HCPB) breeder blanket concept for DEMO will use advanced ceramic breeder (ACB) pebbles consisting of 65 mol% lithium orthosilicate (Li_4SiO_4) and 35 mol% lithium metatitanate (Li_2TiO_3) as tritium breeding material [3,4]. Along with the main task of producing and releasing tritium, the biphasic ACB pebbles must also withstand expected harsh operational conditions, e.g., intense neutron radiation, elevated temperature, high magnetic field, etc. [5]. Therefore, few neutron irradiation experiments with various parameters have already been performed for the ACB pebbles, and the release behaviour of the generated tritium and helium by nuclear transmutation reactions has been investigated in *in-situ* [6] and *ex-situ* modes [7]. Previously, several authors have reported that radiation-induced defects (simple centres), their aggregates (complex centres), and radiolysis products formed and

* Corresponding author at: University of Latvia, Institute of Chemical Physics, 1 Jelgavas Str., LV-1004 Riga, Latvia.
E-mail address: arturs.zarins@lu.lv (A. Zarins).

https://doi.org/10.1016/j.nme.2024.101698
Received 23 April 2024; Received in revised form 10 June 2024; Accepted 24 June 2024
Available online 25 June 2024

accumulated during neutron irradiation can act as tritium scavenger centres in Li_4SiO_4 and Li_2TiO_3 [8–10]. These centres can considerably affect the diffusion and release processes of the generated tritium. However, it needs to be highlighted that neutron irradiation experiments are time-consuming, the handling and transportation of the neutron-irradiated samples is difficult due to the neutron activation of the material, and the experimental costs are high [11]. Several alternative irradiation sources and ionising radiation of various types, masses, and energies have been used in order to investigate radiation-induced effects in the ACB pebbles: (1) photons (X-rays, gamma rays, and *bremsstrahlung*) with energies up to 6 MeV; (2) electrons (beta particles and accelerated electrons) with energies up to 10 MeV and irradiation temperatures up to 1000 °C; (3) accelerated ions with masses up to 127 amu (hydrogen, deuterium, helium, oxygen, silicon, argon, iron, and iodine) and energies up to 20 MeV [12,13]. Regardless of the type, mass, and energy of ionising radiation, the formation and accumulation of similar paramagnetic radiation-induced defect centres (containing unpaired electrons) have been reported [14].

Electron-nuclear double resonance (ENDOR) spectroscopy is a non-destructive technique that combines the aspects of electron paramagnetic resonance (EPR) and nuclear magnetic resonance (NMR) [15]. Recently, EPR spectroscopy was used to separate individual signals of paramagnetic centres in the ACB pebbles after irradiation with X-rays by EPR spectra simulations [14]. Multiple signals of electronic spin $S = 1/2$ centres with distinctive symmetries and g-factor (g) values were identified and characterised. It was concluded that the Li_2TiO_3 phase introduces a variety of electron traps in the primary Li_4SiO_4 phase of the ACB pebbles, which form the detected paramagnetic centres with EPR signals in the $g < 2.00$ region after irradiation. Nevertheless, it was noted that the assignment of these EPR signals to specific paramagnetic centres is problematic. In order to characterise hyperfine (HF) interactions of the unpaired electronic spins with the spins of magnetic nuclei ($I \neq 0$), ENDOR spectroscopy can be applied. During continuous-wave (CW) ENDOR spectra measurements, a specific EPR signal is monitored at a fixed magnetic field and microwave (MW) frequency to excite unpaired electron spin transitions, while a second radio frequency (RF) source excites NMR transitions of the neighbouring magnetic nuclei. Magnetic isotopes of ^{6}Li ($I = 1$), ^{29}Si ($I = 1/2$), ^{47}Ti ($I = 5/2$), ^{49}Ti ($I = 7/2$), and ^{17}O ($I = 5/2$) have low natural abundance (~7.5 %, 4.7 %, 7.4 %, 5.4 %, and 0.04 %, respectively). Therefore, the detection of ENDOR signals associated with ^{7}Li isotope nuclei ($I = 3/2$, abundance: ~92.5 %) is mainly expected [16] for the ACB pebbles after irradiation.

In the present work, ENDOR spectroscopy was used to investigate HF interactions of paramagnetic centres in the ACB pebbles after irradiation with 10 MeV accelerated electrons. The irradiation experiment with accelerated electrons instead of neutrons was selected in order to induce the formation and accumulation of paramagnetic centres due to direct ionisation, excitation (radiolysis), and single atomic displacements, while avoiding neutron activation, lithium burn-up, and generation of tritium and helium [17]. To separate individual EPR signals of the paramagnetic centres, X- and Q-band EPR spectra at room temperature (RT) and 80 K as well as X-band ENDOR spectra at 10 K were recorded for the irradiated ACB pebbles before and after isochronal annealing from RT up to 300 °C. To highlight the distinction between EPR and ENDOR spectra acquisition temperature and sample annealing temperature, the acquisition temperature is indicated in Kelvin, while the annealing temperature in degrees Celsius. Afterwards, EPR and ENDOR spectra simulations were performed to determine the g values and HF coupling values of the paramagnetic centres.

Experimental

The ACB pebbles with a nominal composition of 65 mol% Li_4SiO_4 and 35 mol% Li_2TiO_3 were produced using the KALOS (**KA**rlsruhe **L**ithium **O**rtho**S**ilicate) process [5]. Based on the determined content of silicon and titanium using inductively coupled plasma – optical emission spectrometry (ICP-OES, iCAP 7600 – ThermoFisher-Scientific), the actual composition of the produced ACB pebbles is evaluated to be 65.3 mol% Li_4SiO_4 and 34.7 mol% Li_2TiO_3. The microstructure and crystalline phase composition of the ACB pebbles, which have been produced using the KALOS process with similar chemical composition, have already been characterised and described in detail by Leys et al. [18] and Heuser et al. [19]. Typically, the ACB pebbles have a dendritic structure of two crystalline phases: monoclinic Li_4SiO_4 and cubic high-temperature Li_2TiO_3. The dominating metallic impurity usually is aluminium (<0.1 wt%) with only one stable and magnetic isotope (^{27}Al, $I = 5/2$, abundance: 100 %), which is introduced in the ACB pebbles during the production process from raw materials [20]; nevertheless, characteristic EPR signals in the $g > 2.00$ range of paramagnetic aluminium-related hole-type centres were not detected for the ACB pebbles after irradiation with X-rays [14]. The content of other metallic impurities with magnetic nuclei, e.g., platinum (^{195}Pt, $I = 1/2$, abundance: ~33.8 %), gold (^{197}Au, $I = 3/2$, abundance: 100 %), potassium (^{39}K, $I = 3/2$, abundance: ~93.26 %; ^{40}K, $I = 4$, abundance: ~0.01 %; ^{41}K, $I = 3/2$, abundance: ~6.73 %), sodium (^{23}Na, $I = 3/2$, abundance: 100 %), etc., is much smaller in comparison to aluminium impurities in the ACB pebbles; therefore, it is expected that the influence of these impurities on the EPR and ENDOR spectra measurements will be negligible.

For transportation and irradiation, the produced ACB pebbles were inserted into a plastic bottle and afterwards sealed into a vacuumed plastic bag in order to avoid reactions on the pebble surface with water (H_2O) vapour and carbon dioxide (CO_2) from air [21]. Hydrogen has two stable isotopes with magnetic nuclei: ^{1}H ($I = 1/2$, abundance: ~99.985 %) and ^{2}H ($I = 1$, abundance: ~0.015 %), while carbon has one magnetic isotope (^{13}C, $I = 1/2$, abundance: ~1.06 %).

The irradiation was performed stepwise using 10 MeV accelerated electrons up to 0.5 MGy absorbed dose with an incremental step of 25 kGy at RT in air with a linear electron accelerator "Elektronika 10/10" [22,23]. The irradiation temperature during each irradiation cycle was below 50 °C, which was determined on the basis of calorimetric (graphite) measurements. Before characterisation, the irradiated sealed vacuumed plastic bag was opened and afterwards the irradiated ACB pebbles were stored in a plastic bottle using desiccator cabinet at RT (~20–25 °C) in air with low relative humidity (~10 RH%). According to the previously obtained results of irradiation experiments with 5 MeV accelerated electrons at various conditions [24,25], it is expected that the microstructure and crystalline phase composition of the ACB - pebbles will not significantly change during irradiation with such intermediate absorbed dose at RT.

CW EPR spectra were recorded for the irradiated ACB pebbles with a Bruker ELEXSYS-II E500 CW-EPR system (Bruker Biospin, Rheinstetten, Germany). Three different spectrometer operation modes were used: (1) X-band MW frequency (9.832 GHz) at RT (~297 K); (2) X-band MW frequency (9.362 GHz) at 80 K; (3) Q-band MW frequency (33.90 GHz) at RT. 10 mW MW power was used for measurements at RT and 0.1 mW – for measurements at 80 K. The magnetic field modulation parameters were 100 kHz frequency and 0.1 mT amplitude. Isochronal sample annealing was performed from RT up to 300 °C in a custom-built furnace with an estimated temperature uncertainty of ± 10 °C, maintaining each annealing step for 10 min.

ENDOR spectra were acquired with the same Bruker ELEXSYS-II E500 CW-EPR system equipped with DICE-II CW ENDOR measurement system and Bruker EN 901 X-Band CW-ENDOR resonator mounted on an Oxford Instruments liquid helium flow cryostat. The temperature during data acquisition was 10 K; static magnetic field values were 340.993 mT and 353.527 mT. The MW frequency was 9.571 GHz at 5 mW power. The RF modulation type was frequency modulation (FM) with 200 kHz modulation depth. The resulting spectra are a sum of 4 ENDOR scans.

For EPR and ENDOR spectra simulations, EasySpin software [26] was used. The experimental magnetic field and frequency values stated

above were used in the simulations. The EPR spectra were simulated as a superposition of individual signals originating from electronic spin $S = 1/2$ centres with rhombic symmetry g-factor ($g_1 \neq g_2 \neq g_3$). ENDOR signals were calculated from 1 to 31 MHz with 1000 points at magnetic field values of 341 mT and 354 mT, respectively. For ENDOR spectra analysis, anisotropic HF interactions ($A_1 \neq A_2 \neq A_3$) with ^{1}H ($I = 1/2$) and ^{7}Li ($I = 3/2$) nuclei were considered. Functions provided by EasySpin were utilised to calculate powder CW EPR and ENDOR spectra and modified to provide parallelisation and fitting with the built-in least squares fitting algorithm. Sufficiently high simulation step was chosen so that it does not affect the result and increased further for display purposes.

Results and discussion

A RT X-band EPR spectrum of the electron-irradiated ACB pebbles is shown in Fig. 1. The detected EPR spectrum consists of several signals in the proximity of the free electron $g_e = 2.0023$ value (at 350 mT), which is consistent with the results reported for the ACB pebbles produced using the KALOS process after exposure to different types of ionising radiation [14,24,25]. Paramagnetic centres can be differentiated based on the shift of the g value from the g_e value to interpret the nature of radiation-induced defect centres. Due to a negative spin-coupling value, hole-type centres (HCs) generally have $g > g_e$ and are shifted towards lower magnetic fields, while the opposite ($g < g_e$) is true for electron-type centres (ECs), and the respective signals are located at higher field values [27,29]. As the irradiated ACB pebbles were stored in a desiccator cabinet for several months before EPR analysis, the least stable HC signals in the $g = 2.04$–2.02 range [14,24] have already decayed, and only the signals that are stable at RT remain. It has been demonstrated that a variety of HCs are generated in the primary Li_4SiO_4 phase of the ACB pebbles during irradiation [17,25,28], whereas the second Li_2TiO_3 phase exhibits higher radiation stability [28]. However, it has been suggested that the introduction of Li_2TiO_3 in the ACB pebbles promotes the creation of electron traps within crystalline structure of the Li_4SiO_4 phase, possibly, due to the incorporation of titanium in negligible amounts during the production process, which form the detected ECs after exposure to ionising radiation [14].

Fig. 2 presents a comparison of EPR spectra of the irradiated ACB pebbles acquired in different detection modes following stepwise isochronal annealing at selected temperatures. Prior to the EPR measurements, the relatively unstable paramagnetic centres have already decayed, resulting in minimal changes after annealing up to 100 °C. Gradual decay in the 100–300 °C range is consistent with the annealing curves reported by several groups of researchers [14,25,28]. The complex evolution of EPR spectra at higher annealing temperatures can only be explained by a superposition of overlapping signals originating from multiple paramagnetic centres.

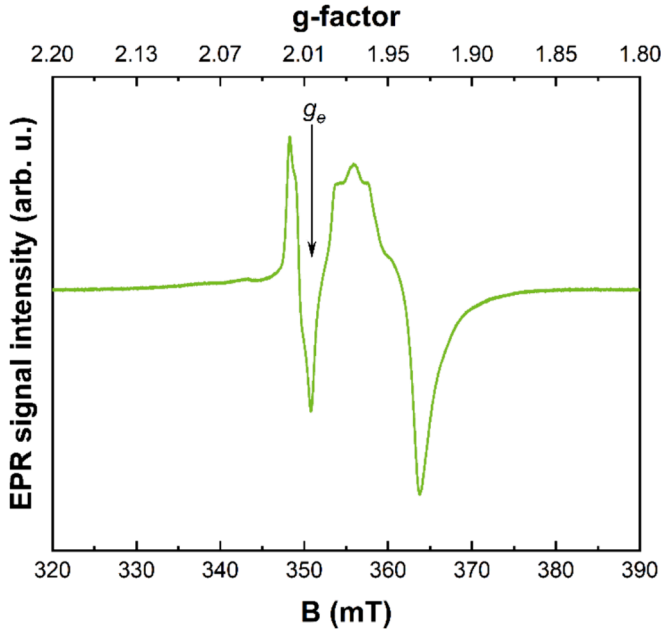

Fig. 1. RT X-band EPR spectrum of the electron-irradiated ACB pebbles.

Multiple EPR spectra acquisition parameters such as measurement temperature and MW frequency provide useful experimental data for determining spin-Hamiltonian (SH) parameters of individual paramagnetic centres via EPR spectra simulations. The low-temperature signals (Fig. 2 **(b)**) are better resolved in comparison to RT-detected counterparts (Fig. 2 **(a)**); moreover, the relative intensity variations of the signals corroborate the different origins of the HCs and ECs. The Q-band EPR spectra (Fig. 2 **(c)**) reveal that the magnetic field range of the observed resonances scales with MW frequency, which implies that the shape of individual EPR signals is governed by g value anisotropy of electronic spin $S = 1/2$ centres. These effects are clearly illustrated in Fig. 3, where the EPR spectra before the isochronal annealing are compared in the g value scale. This allows us to propose the following SH for the simulations of EPR spectra:

$$H = g\mu_B BS \quad (1)$$

where g is the g-factor; μ_B – the Bohr magneton; B – external magnetic field; S – electronic spin operator [29].

Simulations of the RT EPR spectra acquired at different MW frequencies before the isochronal annealing shown in Fig. 4 reveal that the $g > g_e$ region can be satisfactorily explained by a single paramagnetic centre (in further text abbreviated as HC I) with the determined SH parameters listed in Table 1. Due to the scaling of the Zeeman effect with magnetic field, g value anisotropy is better resolved at higher MW frequency. Within the margins of uncertainty, the determined SH parameters of HC I are coincident with one of HCs reported in photon-irradiated Li_4SiO_4 pebbles produced with a 2.5 wt% surplus of silicon dioxide (SiO_2) [17]. This result implies a similar model for the HC I, i.e., a hole trapped at an oxygen ion resulting in the formation of O^--type centre in the primary Li_4SiO_4 phase of the ACB pebbles. This hypothesis is based on the detection of an EPR signal with similar g-factor values and annealing characteristics in SiO_2-based glasses [30]. However, in the structure of Li_4SiO_4, the influence of lithium atoms on the trapping of holes should also be considered.

After isochronal annealing at a sufficiently high temperature (200–250 °C), the EC region of the EPR spectra can be simulated by a single centre, which is shown in Fig. 5. The RT-detected EPR spectrum is essentially the same as for one of ECs (abbreviated EC II), which was separated for the ACB pebbles after irradiation with X-rays [14]. Nevertheless, such a simplified model of EC II cannot fully explain the line-shape of the low-temperature-detected spectrum of the irradiated ACB pebbles suggesting the overlap of several stable ECs. Additionally, a remnant of the HC I signal remains, which is superimposed by an isotropic line at $g = 2.00$. Similar signals have previously been interpreted as E'-type centres (in the simplest case, an unpaired electron localised on a dangling tetrahedral (sp^3) orbital of a single silicon atom) [14,28].

The extracted signals outlined above are combined in Fig. 6 to obtain a tentative simulation spectrum of the irradiated ACB pebbles before the isochronal annealing. The HC I and EC II components were determined reliably from the annealing experiments in different EPR spectra acquisition modes (Fig. 2) and are consistent with previous studies [14,17]. Evidently, these signals alone are not sufficient to account for all features of the experimentally obtained spectrum, and additional components are required. An isotropic component with $g = 2.00$ notably enhances the agreement between the experimental and simulation spectra. Structureless signals near the g_e value after exposure to ionising

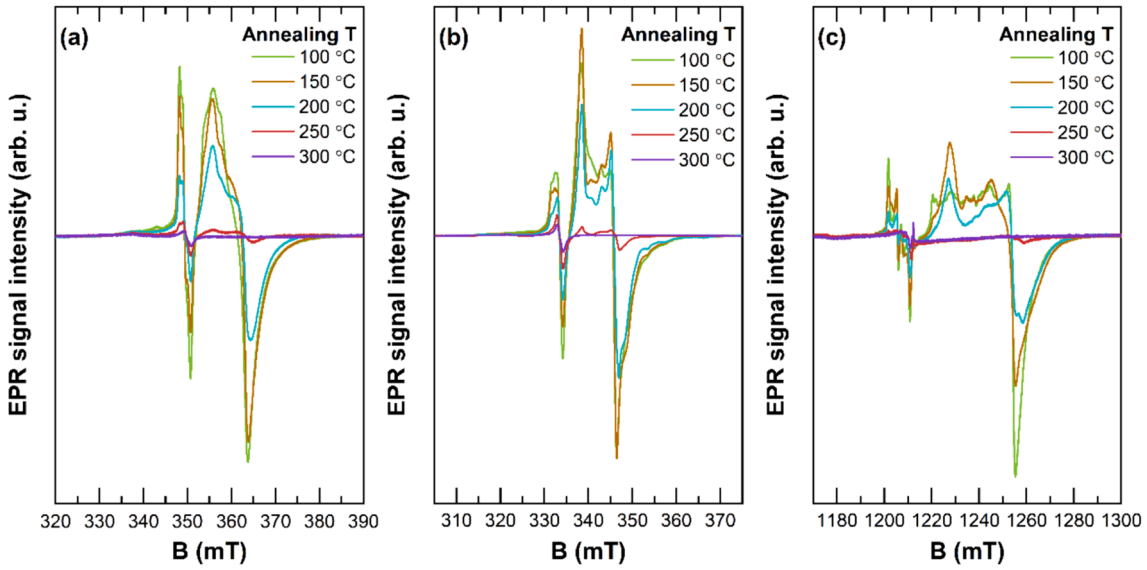

Fig. 2. EPR spectra of the irradiated ACB pebbles after isochronal annealing at selected temperatures: **(a)** X-band MW frequency at RT; **(b)** X-band MW frequency at 80 K; **(c)** Q-band MW frequency at RT.

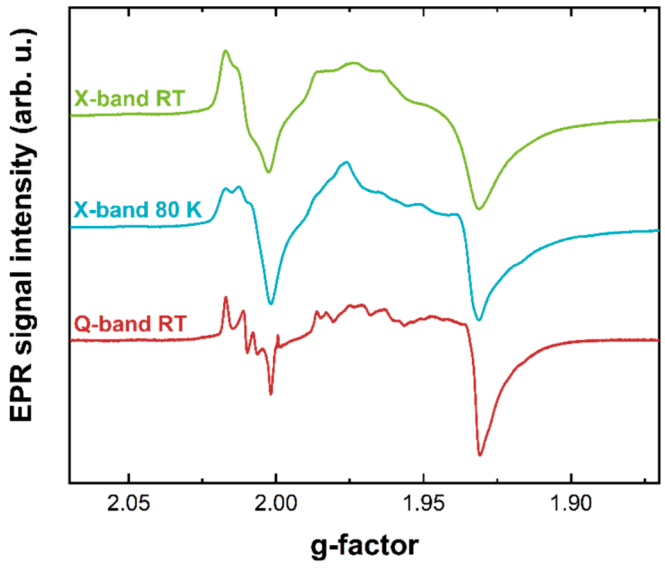

Fig. 3. EPR spectra in g value scale for the irradiated ACB pebbles before isochronal annealing.

radiation are ubiquitously observed in various hosts, including Li_4SiO_4, Li_2TiO_3, and biphasic ACB pebbles [14,17,24,25,28], and are therefore problematic to correctly interpret. To improve the result of least squares fitting of the experimental spectrum in the $g < g_e$ range, an additional component ascribed to EC III was included. It should be noted that this simulation is not unambiguous and cannot completely explain the intricate annealing behaviour of EPR spectra recorded in different settings (Fig. 2). The existence of multiple simulation solutions for the experimental spectra, which are composed of broad and overlapping signals, demonstrates the limitations of conventional CW-EPR spectroscopy and highlights the requirement for more advanced experimental techniques.

ENDOR spectroscopy was applied to gain insights into the HF interactions of paramagnetic centres in the irradiated ACB pebbles. A summary of ENDOR investigations is provided in Fig. 7. CW-ENDOR requires power saturation of the EPR signal; therefore, low temperature and high MW power were used to detect the EPR spectrum (Fig. 7 **(a)**). Field positions in the EPR spectrum marked as "ENDOR 1" and "ENDOR 2" were selected, which correspond to HCs (Fig. 7 **(b)**) and ECs (Fig. 7 **(c)**), respectively. By fixing the static magnetic field onto a saturated EPR signal and simultaneous scanning of an RF source, ENDOR spectra were acquired. To account for interactions between the electronic spin S and the spins of magnetic nuclei I, the following SH was used:

$$H = g\mu_B BS + \sum_{i=1}^{n} hSA_iI_i - \sum_{i=1}^{n} \mu_N g_N BI_i \quad (2)$$

where A – HF interaction tensor; μ_N – nuclear magneton; g_N – nuclear g-factor [29]. In Eq. (2), the first term represents the electron Zeeman interaction; the second – the HF interaction between S and i^{th} nucleus; and the third – the nuclear Zeeman interaction.

The type of interacting nuclei and the interaction strength with the paramagnetic centre can be determined from CW-ENDOR spectra. Isotopes exhibit characteristic ENDOR peaks at a given field value predicted by the g_N values, which are tabulated in the literature, according to the third term of Eq. (2). The intensity distributions for the same element isotopes generally reflect their natural abundances. In the case of HF interaction, a splitting of ENDOR peaks is observed. The A values characterise the HF splitting in MHz of the electron spin levels; higher values tend to indicate decreased distance between the unpaired spin and the nucleus.

The ENDOR 1 spectrum corresponding to HCs (Fig. 7 **b**) consists of three symmetric singlet lines, which are centred at 2.1, 5.6, and 14.6 MHz. For the static magnetic field of 341 mT, these values correspond to the natural Larmor frequencies of ^{6}Li, ^{7}Li and ^{1}H nuclei, respectively. This implies that the HF interaction between the unpaired spin and these nuclei is insignificant (i.e., $A \approx 0$ MHz), suggesting that these nuclei are not located in a direct vicinity of the paramagnetic centre. Due to the low natural abundance of the ^{6}Li isotope and considerable background noise, this line is not resolved in the experimental spectrum.

The ENDOR 2 spectrum corresponding to the ECs (Fig. 7 **(c)**) exhibits a more complicated pattern. The signals are slightly shifted towards higher frequencies and split into multiple components. The components are centred around the natural Larmor frequencies of ^{7}Li and ^{1}H nuclei with a splitting of A. For the interaction with the ^{1}H nucleus, the splitting is not entirely symmetric, which implies anisotropy of the HF interaction tensor. The following A values were determined from ENDOR spectra simulations: $A_1^{1H} = 2.2 \pm 0.2$ MHz, $A_2^{1H} = 0.7 \pm 0.2$

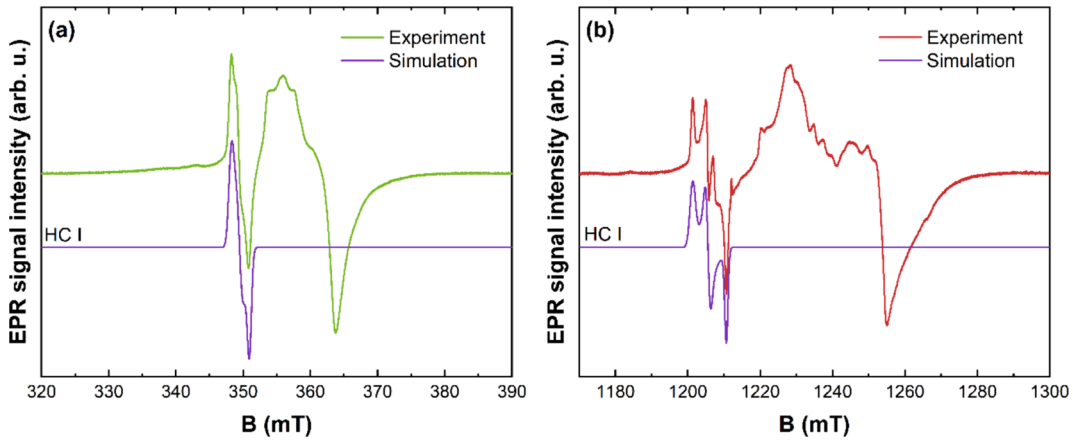

Fig. 4. Simulations of RT EPR spectra for the irradiated ACB pebbles obtained at **(a)** X-band and **(b)** Q-band MW frequencies before isochronal annealing.

Table 1
Determined SH parameters of the paramagnetic radiation-induced defect centres in the ACB pebbles.

Centre	$g_1 \pm 0.0010$	$g_2 \pm 0.0010$	$g_3 \pm 0.0010$
HC I	2.0175	2.0105	2.0004
EC II	1.9759	1.9330	1.9229
EC III	1.9766	1.9380	1.9332
$g = 2.00$	2.0053		

MHz, and $A_3^{1H} = 0.4 \pm 0.2$ MHz.

Simulations of the ^{7}Li ENDOR spectra converged on two different solutions (not including the central $A^{7Li} = 0$ MHz line). The first model assumes isotropic HF interaction constants between the unpaired spin and three distinct ^{7}Li nuclei (2.1, 1.5, and 1.0 MHz, respectively). In the second model, which is shown as the simulation curve in Fig. 7 **(c)**, there is anisotropic HF interaction with a single ^{7}Li nucleus ($A_1^{7Li} = 2.6 \pm 0.2$ MHz, $A_2^{7Li} = 0.9 \pm 0.2$ MHz, and $A_3^{7Li} = 0.7 \pm 0.2$ MHz). Both simulation models offer excellent least squares fitting results of the experimental ENDOR spectrum; therefore, additional investigations are necessary to resolve the uncertainty of the simulation results. Moreover, as demonstrated in Fig. 6, at least two paramagnetic centres contribute to the EPR spectrum at the magnetic field position at which the ENDOR 2 signal was acquired. This suggests that the experimental ENDOR spectrum is a superposition of signals from different ECs.

A discussion regarding the nature of ECs in the irradiated ACB pebbles can be initiated notwithstanding the interpretation ambiguity of ENDOR results. It has been proposed by Zarins et al. [14] that the EC signals originate from the titanium impurities introduced in the crystalline structure of primary Li_4SiO_4 phase of the ACB pebbles. The detection of multiple ^{7}Li ENDOR signals in the present work further supports the idea of assigning ECs to the lithium-rich phase of the ACB pebbles. EPR signals with comparable g values and ^{7}Li HF interaction matrices have been observed in α-quartz (SiO_2) [31–33]. The precursor of these ECs in SiO_2 are Ti^{4+} ions which substitute silicon sites forming $[TiO_4]^0$ tetrahedra. After exposure to X-rays, these sites trap electrons formed by direct ionisation leading to a change in the oxidation state of titanium from +4 to +3. Based on the mechanism of charge compensation, a variety of paramagnetic titanium-related ECs, which are shown in Table 2 in overview, have been documented. Hydrogen- and lithium-compensated titanium-related ECs have also been reported in rutile (TiO_2) [34–36].

A few restricting remarks must be made while comparing the SH parameters of the irradiated ACB pebbles with titanium-related ECs in SiO_2 and TiO_2 in the assignment of the observed ECs to similar paramagnetic centres. Firstly, the studies outlined above were conducted on single crystals enabling precise determination of g and A matrices from EPR/ENDOR signal angular dependences. In contrast, investigations of the irradiated ACB pebbles, a multi-phase ceramic, result in orientation-averaged EPR/ENDOR spectra, which possibly also originate from paramagnetic centres in different crystalline phases. Secondly, it remains uncertain whether the simultaneous detection of ENDOR signals from both ^{1}H and ^{7}Li nuclei can be attributed to a single EC or different paramagnetic centres with overlapping EPR signals. Finally, the detection of EPR signals corresponding to ECs in the irradiated ACB pebbles at RT is perplexing, as the titanium-related ECs EPR spectra are typically

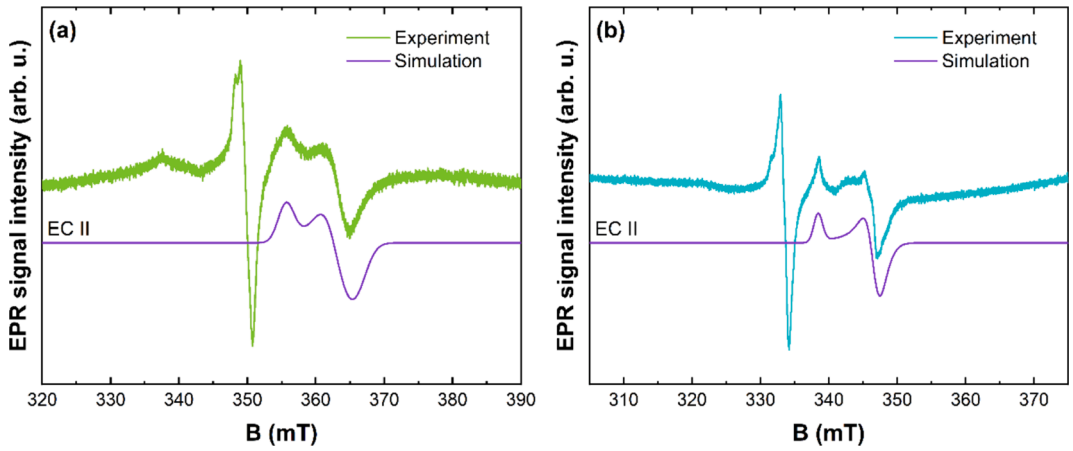

Fig. 5. Simulations of X-band EPR spectra for the irradiated ACB pebbles obtained at **(a)** RT and **(b)** 80 K after isochronal annealing at 250 °C.

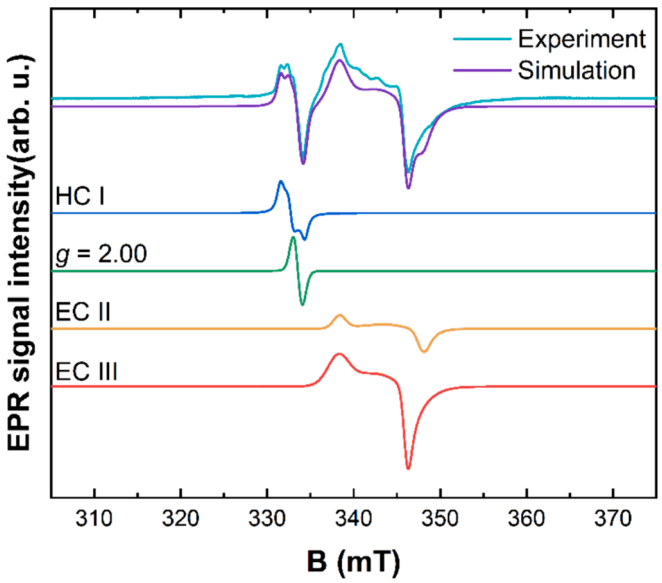

Fig. 6. Simulations of the experimental X-band EPR spectrum for the irradiated ACB pebbles acquired at 80 K before the isochronal annealing as a superposition of individual signals.

detected in the low-temperature range [31,32,34,35]. Therefore, it would be of scientific interest to further study single-phase titanium-doped Li_4SiO_4 and lithium-doped Li_2TiO_3 ceramics in order to establish the local structure of paramagnetic centres in these materials.

Conclusions

EPR and ENDOR spectroscopy techniques were combined to elucidate the local structure of paramagnetic radiation-induced defect centres (containing unpaired electrons) in the biphasic ACB pebbles consisting of 65 mol% Li_4SiO_4 and 35 mol% Li_2TiO_3. After irradiation with 10 MeV accelerated electrons, at least four room-temperature-stable electronic spin $S = 1/2$ centres are formed in the structure of the investigated material. The paramagnetic centres exhibit overlapping EPR spectra with signal shapes governed by g-factor anisotropy and ENDOR signals with the spins of magnetic ^{7}Li and ^{1}H isotope nuclei. The hyperfine interaction between the hole-type centres and magnetic nuclei was not detected ($A \approx 0$ MHz), suggesting that these nuclei are not located in a direct vicinity of the paramagnetic centres. The ENDOR signals of electron-type centres suggest that ^{7}Li ($A_1^{7Li} = 2.6$ MHz, $A_2^{7Li} = 0.9$ MHz, and $A_3^{7Li} = 0.7$ MHz) and ^{1}H ($A_1^{1H} = 2.2$ MHz, $A_2^{1H} = 0.7$ MHz, and $A_3^{1H} = 0.4$ MHz) nuclei are directly interacting with these paramagnetic centres. Comparable g-factor values and hyperfine interaction matrices have been reported in the scientific literature for hydrogen- and lithium-compensated titanium-related electron-type centres in quartz and rutile. The obtained results provide novel fundamental insights into the local structure of paramagnetic centres, which can form in the tritium breeding material during exposure to ionising radiation when used in a fusion reactor.

CRediT authorship contribution statement

Andris Antuzevics: Writing – review & editing, Methodology, Investigation, Conceptualization, Writing – original draft. **Arturs Zarins:** Writing – review & editing, Writing – original draft, Supervision,

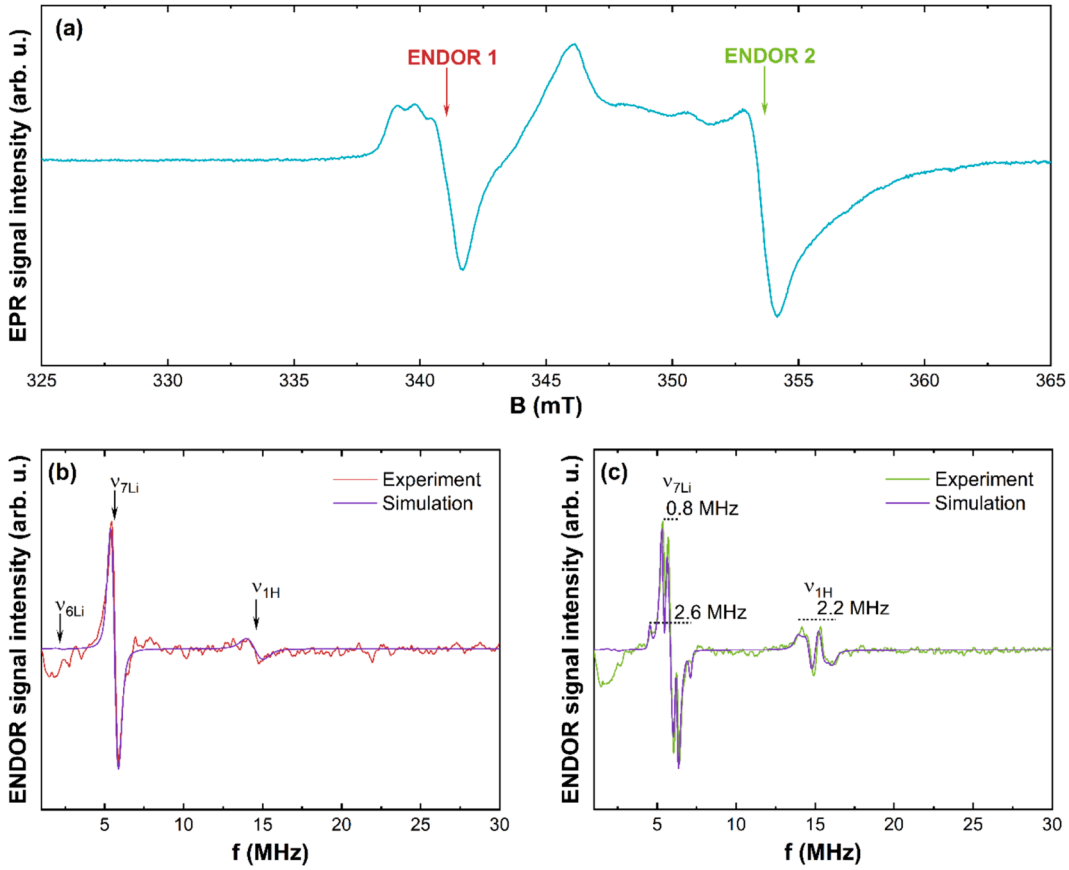

Fig. 7. ENDOR analysis of the irradiated ACB pebbles: **(a)** experimental EPR spectrum; experimental and simulation ENDOR spectra acquired at **(b)** 341.0 mT (corresponding to ENDOR 1); **(c)** 353.5 mT (ENDOR 2).

Table 2
A comparison of *g* values and HF matrices of lithium- and hydron-related ECs in various hosts. *The *g* values were evaluated as the average value for ECs from Table 1.

Host	Centre	g-factor (*g*)	HF matrix	Reference
ACB pebbles *(65 mol% Li_4SiO_4 + 35 mol% Li_2TiO_3)*	EC	*	^{7}Li $A_1 = 2.6$ MHz $A_2 = 0.9$ MHz $A_3 = 0.7$ MHz ^{1}H $A_1 = 2.2$ MHz $A_2 = 0.7$ MHz $A_3 = 0.4$ MHz	Present study
SiO_2 (α-quartz)	$[TiO_4/Li]^0_A$	$g_1 = 1.97887$ $g_2 = 1.93094$ $g_3 = 1.91193$	^{7}Li $A_1 = 7.54$ MHz $A_2 = 3.60$ MHz $A_3 = 3.09$ MHz	[31,33]
	$[TiO_4/Li]^0_B$	$g_1 = 1.98022$ $g_2 = 1.92977$ $g_3 = 1.91022$	^{7}Li $A_1 = 4.51$ MHz $A_2 = 0.02$ MHz $A_3 = -0.08$ MHz	[32,33]
	$[TiO_4/H]^0_A$	$g_1 = 1.9856$ $g_2 = 1.9310$ $g_3 = 1.9151$	^{1}H $A_1 = 26.3$ MHz $A_2 = 12.8$ MHz $A_3 = 12.2$ MHz	[33]
	$[TiO_4/H]^0_B$	$g_1 = 1.990$ $g_2 = 1.914$ $g_3 = 1.903$	^{1}H $A_1 = 25.6$ MHz $A_2 = 14.3$ MHz $A_3 = 13.3$ MHz	[33]
TiO_2 (rutile)	Ti^{3+}-Li^+	$g_1 = 1.9688$ $g_2 = 1.9204$ $g_3 = 1.9323$	^{7}Li $A_1 = -2.12$ MHz $A_2 = -2.20$ MHz $A_3 = +3.44$ MHz	[34]
	Ti^{3+} adjacent to OH^-	$g_1 = 1.9732$ $g_2 = 1.9765$ $g_3 = 1.9405$	^{1}H $A_1 = -0.401$ MHz $A_2 = 0.616$ MHz $A_3 = -0.338$ MHz	[35,36]

Project administration, Methodology, Investigation, Funding acquisition, Formal analysis, Conceptualization. **Jekabs Cirulis:** Writing – review & editing, Methodology, Investigation, Conceptualization. **Andris Fedotovs:** Writing – review & editing, Methodology, Investigation, Conceptualization. **Anna Ansone:** Writing – review & editing, Methodology, Investigation, Conceptualization. **Magdalena Rzepna:** Writing – review & editing, Methodology, Investigation, Conceptualization. **Julia M. Leys:** Writing – review & editing, Resources, Conceptualization. **Regina Knitter:** Writing – review & editing, Resources, Conceptualization.

Declaration of competing interest

The authors declare that they have no known competing financial interests or personal relationships that could have appeared to influence the work reported in this paper.

Data availability

Data will be made available on request.

Acknowledgements

This work has been carried out within the framework of the EUROfusion Consortium, funded by the European Union via the Euratom Research and Training Programme (Grant Agreement No 101052200 – EUROfusion). Views and opinions expressed are however those of the author(s) only and do not necessarily reflect those of the European Union or the European Commission. Neither the European Union nor the European Commission can be held responsible for them.

Institute of Solid State Physics, University of Latvia as the Center of Excellence has received funding from the European Union's Horizon 2020 Framework Programme H2020-WIDESPREAD-01-2016-2017-TeamingPhase2 under grant agreement No. 739508, project CAMART2.

References

[1] E.G. Carayannis, M. Vincenzi, J. Draper, The economic logic of open science in fusion energy research: a policy perspective, Energy Policy 186 (2024) 113983, https://doi.org/10.1016/j.enpol.2024.113983.
[2] M. Zaupa, M.D. Palma, I. Moscato, L. Barucca, Balance of plant conceptual design of EU DEMO integrating different breeding blanket concepts, Fusion Eng. Des. 200 (2024) 114235, https://doi.org/10.1016/j.fusengdes.2024.114235.
[3] L.V. Boccaccini, F. Arbeiter, P. Arena, J. Aubert, L. Bühler, I. Cristescu, A. Del Nevo, M. Eboli, L. Forest, C. Harrington, F. Hernandez, R. Knitter, H. Neuberger, D. Rapisarda, P. Sardain, G.A. Spagnuolo, M. Utili, L. Vala, A. Venturini, P. Vladimirov, G. Zhou, Status of maturation of critical technologies and systems design: breeding blanket, Fusion Eng. Des. 179 (2022) 113116, https://doi.org/10.1016/j.fusengdes.2022.113116.
[4] G. Zhou, F.A. Hernández, P. Pereslavtsev, B. Kiss, A. Retheesh, L. Maqueda, J. H. Park, The European DEMO helium cooled pebble bed breeding blanket: design status at the conclusion of the pre-concept design phase, Energies 16 (2023) 5377, https://doi.org/10.3390/en16145377.
[5] O. Leys, J.M. Leys, R. Knitter, Current status and future perspectives of EU ceramic breeder development, Fusion Eng. Des. 164 (2021) 112171, https://doi.org/10.1016/j.fusengdes.2020.112171.
[6] T. Kulsartov, Z. Zaurbekova, R. Knitter, I. Kenzhina, Y. Chikhray, A. Shaimerdenov, S. Askerbekov, G. Kizane, A. Yelishenkov, T. Zholdybayev, Comparative analysis of gas release from biphasic lithium ceramics pebble beds of various pebbles sizes and content under neutron irradiation conditions, Nuclear Materials and Energy 38 (2024) 101583, https://doi.org/10.1016/j.nme.2024.101583.
[7] Y. Chikhray, S. Askerbekov, R. Knitter, T. Kulsartov, A. Shaimerdenov, M. Aitkulov, A. Akhanov, D. Sairanbayev, Z. Bugybay, A. Nessipbay, K. Kisselyov, G. Kizane, A. Zarins, Studies of irradiated two-phase lithium ceramics Li_4SiO_4/Li_2TiO_3 by thermal desorption spectroscopy, Nuclear Materials and Energy 38 (2024) 101621, https://doi.org/10.1016/j.nme.2024.101621.
[8] Y. Nishikawa, M. Oyaidzu, A. Yoshikawa, K. Munakata, M. Okada, M. Nishikawa, K. Okuno, Correlation between tritium release and thermal annealing of irradiation damage in neutron-irradiated Li_2SiO_3, J. Nucl. Mater. 367–370 (2007) 1371–1376, https://doi.org/10.1016/j.jnucmat.2007.03.251.
[9] M. Kobayashi, Y. Oya, K. Munakata, K. Okuno, Developing a tritium release model for Li_2TiO_3 with irradiation-induced defects, J. Nucl. Mater. 458 (2015) 22–28, https://doi.org/10.1016/j.jnucmat.2014.11.047.
[10] G. Kizane, J. Tiliks, A. Vitins, J. Rudzitis, Tritium localisation and release from the ceramic pebbles of breeder, J. Nucl. Mater. 329–333 (2004) 1287–1290, https://doi.org/10.1016/j.jnucmat.2004.04.229.
[11] J.M. Leys, A. Zarins, J. Cipa, L. Baumane, G. Kizane, R. Knitter, Radiation-induced effects in neutron- and electron-irradiated lithium silicate ceramic breeder pebbles, J. Nucl. Mater. 540 (2020) 152347, https://doi.org/10.1016/j.jnucmat.2020.152347.
[12] A. Zarins, A. Ansone, M. Senko, J. Cipa, A. Antuzevics, L. Avotina, L. Baumane, G. Kizane, M. Gonzalez, J.M. Leys, R. Knitter. Influence of various radiation types on radiation-induced processes in lithium orthosilicate-based ceramic breeder materials. Proceedings of 21st International Workshop on the Ceramic Breeder Blanket Interactions (CBBI-21), 19-20 October 2023, Granada, Spain, p. 576-591.

https://indico.ifmif-dones.es/event/12/attachments/64/457/CBBI-21_Proceedings_2023.pdf.
[13] G. Delgado, M. González. Secondary Ion Mass Spectrometry (SIMS) as an important tool to track compositional variations from ion-implanted and ion-damaged Advance Ceramic Breeder (ACB) compositions. Proceedings of 21st International Workshop on the Ceramic Breeder Blanket Interactions (CBBI-21), 19-20 October 2023, Granada, Spain, p. 592-609. https://indico.ifmif-dones.es/event/12/attachments/64/457/CBBI-21_Proceedings_2023.pdf.
[14] A. Zarins, A. Antuzevics, G. Kizane, J.M. Leys, R. Knitter, Simulations of complex electron paramagnetic resonance spectra for radiation-induced defect centres in advanced ceramic breeder pebbles, Nuclear Materials and Energy 35 (2023) 101458, https://doi.org/10.1016/j.nme.2023.101458.
[15] L. Kulik, W. Lubitz, Electron-nuclear double resonance, Photosynth. Res. 102 (2009) 391–401, https://doi.org/10.1007/s11120-009-9401-y.
[16] I.A. Shkrob, B.M. Tadjikov, A.D. Trifunac, Magnetic resonance studies on radiation-induced point defects in mixed oxide glasses. II. Spin centers in alkali silicate glasses, J. Non Cryst. Solids 262 (2000) 35–65, https://doi.org/10.1016/S0022-3093(99)00669-9.
[17] A. Antuzevics, A. Zarins, A. Ansone, J. Cipa, G. Kizane, J.M. Leys, R. Knitter, Thermal properties of paramagnetic radiation-induced defects in lithium orthosilicate containing breeder material, J. Nucl. Mater. 565 (2022) 153713, https://doi.org/10.1016/j.jnucmat.2022.153713.
[18] O. Leys, C. Odemer, U. Maciejewski, M.H.H. Kolb, R. Knitter, Microstructure analysis of melt-based lithium orthosilicate/metatitanate pebbles, Practical Metallography 50 (2013) 196–204, https://doi.org/10.3139/147.110194.
[19] J.M. Heuser, M.H.H. Kolb, T. Bergfeldt, R. Knitter, Long-term thermal stability of two-phased lithium orthosilicate/metatitanate ceramics, J. Nucl. Mater. 507 (2018) 396–402, https://doi.org/10.1016/j.jnucmat.2018.05.010.
[20] O. Leys, T. Bergfeldt, M.H.H. Kolb, R. Knitter, A.A. Goraieb, The reprocessing of advanced mixed lithium orthosilicate/metatitanate tritium breeder pebbles, Fusion Eng. Des. 107 (2016) 70–74, https://doi.org/10.1016/j.fusengdes.2016.04.025.
[21] J. Ortiz-Landeros, L. Martínez-dlCruz, C. Gómez-Yáñez, H. Pfeiffer, Towards understanding the thermoanalysis of water sorption on lithium orthosilicate (Li_4SiO_4), Thermochim Acta 515 (2011) 73–78, https://doi.org/10.1016/j.tca.2010.12.025.
[22] A. Iuliano, M. Nowacka, K. Rybak, M. Rzepna, The effects of electron beam radiation on material properties and degradation of commercial PBAT/PLA blend, J. Appl. Polym. Sci. 137 (2020) 48462, https://doi.org/10.1002/app.48462.
[23] M. Siwek, T. Edgecock, A.G. Chmielewski, A. Rafalski, M. Walo, M. Sudlitz, L. Lin, Y. Sun, The potential of electron beams for the removal of microplastics from wastewater and sewage sludge, Environmental Challenges 13 (2023) 100760, https://doi.org/10.1016/j.envc.2023.100760.
[24] J.M. Heuser, A. Zarins, L. Baumane, G. Kizane, R. Knitter, Radiation stability of long-term annealed bi-phasic advanced ceramic breeder pebbles, Fusion Eng. Des. 138 (2019) 395–399, https://doi.org/10.1016/j.fusengdes.2018.12.034.
[25] A. Zarins, O. Valtenbergs, G. Kizane, A. Supe, R. Knitter, M.H.H. Kolb, O. Leys, L. Baumane, D. Conka, Formation and accumulation of radiation-induced defects and radiolysis products in modified lithium orthosilicate pebbles with additions of titanium dioxide, J. Nucl. Mater. 470 (2016) 187–196, https://doi.org/10.1016/j.jnucmat.2015.12.027.
[26] S. Stoll, A. Schweiger, EasySpin, a comprehensive software package for spectral simulation and analysis in EPR, J. Magn. Reson. 178 (2006) 42–55, https://doi.org/10.1016/j.jmr.2005.08.013.
[27] A.S. Marfunin. Spectroscopy, luminescence and radiation centers in minerals, 1979. doi: 10.1016/0012-8252(80)90067-7.
[28] B. Ji, S. Gu, Q. Qi, X.-C. Li, Y. Zhang, H. Zhou, G.-N. Luo, Annihilation kinetics of irradiation defects in promising tritium breeding pebbles, Nuclear Materials and Energy 27 (2021) 101015, https://doi.org/10.1016/j.nme.2021.101015.
[29] J.A. Weil, J.R. Bolton, Electron Paramagnetic Resonance, Wiley, 2007.
[30] D.L. Griscom, Electron spin resonance studies of trapped hole centers in irradiated alkali silicate glasses: a critical comment on current models for HC_1 and HC_2, J. Non Cryst. Solids 64 (1984) 229–247, https://doi.org/10.1016/0022-3093(84)90220-5.
[31] J. Isoya, W.C. Tennant, J.A. Weil, EPR of the TiO_4/Li center in crystalline quartz, J. Magn. Reson. 79 (1988) (1969) 90–98, https://doi.org/10.1016/0022-2364(88)90325-3.
[32] P. Bailey, J.A. Weil, EPR of $[TiO_4Li]B^0$ and related centres in X-irradiated α-quartz, J. Phys. Chem. Solid 53 (1992) 601–610, https://doi.org/10.1016/0022-3697(92)90106-N.
[33] R.I. Mashkovtsev, Y. Pan. Nature of paramagnetic defects in α-quartz: Progresses in the First Decade of the 21st Century, in: New Developments in Quartz Research: Varieties, Crystal Chemistry and Uses in Technology, 2013, pp. 65–104.
[34] A.T. Brant, N.C. Giles, L.E. Halliburton, Insertion of lithium ions into TiO_2 (rutile) crystals: an electron paramagnetic resonance study of the Li-associated Ti^{3+} small polaron, J. Appl. Phys. 113 (2013) 053712, https://doi.org/10.1063/1.4790366.
[35] A.T. Brant, S. Yang, N.C. Giles, L.E. Halliburton, Hydrogen donors and Ti^{3+} ions in reduced TiO_2 crystal, J. Appl. Phys. 110 (2011) 053714, https://doi.org/10.1063/1.3630964.
[36] L.E. Halliburton, Electron traps in rutile TiO_2 crystals: intrinsic small polarons, impurities, and oxygen vacancies, Mater. Res. Soc. Symp. Proc. 1731 (2015) 1–12, https://doi.org/10.1557/opl.2015.15.